Journal of Nuclear Materials 569 (2022) 153911

Contents lists available at ScienceDirect

Journal of Nuclear Materials

journal homepage: www.elsevier.com/locate/jnucmat

Mechanical characterisation of V-4Cr-4Ti alloy: Tensile tests under high energy synchrotron diffraction

Tay Sparks[a], Duc Nguyen-Manh[b], Pengfei Zheng[c], Jan S. Wróbel[d], Damian Sobieraj[d], Michael Gorley[b], Thomas Connolley[e], Christina Reinhard[e], Yiqiang Wang[b], Biao Cai[a,*]

[a] School of Metallurgy and Materials, University of Birmingham, Birmingham, United Kingdom
[b] UK Atomic Energy Authority, Culham Science Centre, Abingdon, Oxfordshire OX14 3DB, United Kingdom
[c] Center for Fusion Science of Southwestern Institute of Physics, Chengdu, 610041, China
[d] Faculty of Materials Science and Engineering, Warsaw University of Technology, ul. Wołoska 141, 02-507 Warsaw, Poland.
[e] Diamond Light Source Ltd, Harwell Science and Innovation Campus, Didcot, United Kingdom

ARTICLE INFO

Article history:
Received 29 April 2022
Revised 5 July 2022
Accepted 8 July 2022
Available online 9 July 2022

Key words:
Vanadium alloy
Synchrotron x-ray diffraction
Nuclear materials

ABSTRACT

Vanadium base alloys represent potentially promising candidate structural materials for use in nuclear fusion reactors due to vanadium's low activity, high thermal strength, and good swelling resistance. In this work, the mechanical properties of the current frontrunner vanadium base alloy, V-4Cr-4Ti, have been interrogated using in-situ high energy X-ray diffraction (XRD) tensile testing at varying temperatures. The single crystal elastic constants of the samples were determined from the in-situ XRD data and used to evaluate results from density functional theory calculations. Polycrystalline elastic properties and Zener anisotropy were calculated from the single crystal elastic constants produced, revealing the effect of elevated temperature on the alloy's elastic properties. These results characterise important thermomechanical properties, valuable in mechanical modelling, that will allow further and improved analysis of the structural suitability of V-4Cr-4Ti ahead of alloy adoption in the mainstream.

Crown Copyright © 2022 Published by Elsevier B.V. All rights reserved.

1. Introduction

In recent decades vanadium alloys have become a focus of attention in realising nuclear fusion, exhibiting more favourable activation properties, higher elevated temperature strength and lower swelling rate than reduced activation ferritic martensitic steels [1,2]. These properties mark vanadium alloys as well suited for use as new structural materials in nuclear fusion reactors, which are required to be able to withstand high thermal fluxes, thermal cycling, and irradiation over a long lifetime without suffering structural degradation. Such application would see vanadium employed as a structural support for the self-cooled liquid Li breeder blanket array; attractive as this design is estimated to have a high power efficiency [2], and does not require the use of beryllium as a multiplier – removing the handling difficulties associated with beryllium [3,4].

The vanadium alloy V-4Cr-4Ti weight percent (V44 hereafter) represents a very promising candidate structural material for nuclear fusion reactors; the addition of chromium providing attractive solid solution strengthening, and the addition of titanium suppressing irradiation swelling and impurity embrittlement through the gettering of interstitial impurities into strengthening titanium precipitates (Ti(C,O,N)) [5–7]. Significant research has been conducted over recent years to fully establish the thermomechanical properties of this composition. V44 has been found to exhibit high yield strength to temperatures in excess of 700°C [8,9], maintain its ductility significantly below room temperature [10], and have a viably low thermal expansion coefficient [1] – with these factors cumulatively describing an alloy with highly suitable thermomechanical properties.

In situ diffraction characterisation of tensile samples provides important information as to the lattice dependent physical parameters, in addition to typical mechanical properties. Both X-ray diffraction (XRD) and neutron diffraction are commonly employed to interrogate microstructural properties in this way, but it is notable that neutron diffraction cannot be effectively employed in the characterisation of vanadium-based alloys. This is the result of vanadium's very small coherent scattering cross section, which severely limits results producible from neutron diffraction. Synchrotron high energy XRD, however, can be used to effectively characterise vanadium based alloys, and provides useful information, representative of the bulk sample [11]. Substantial progress has been made over recent decades in the interrogation of such data, allowing for greater insight into the evolution and charac-

* Corresponding author.
E-mail addresses: yiqiang.wang@ukaea.uk (Y. Wang), b.cai@bham.ac.uk (B. Cai).

https://doi.org/10.1016/j.jnucmat.2022.153911
0022-3115/Crown Copyright © 2022 Published by Elsevier B.V. All rights reserved.

ter of microstructural defects during mechanical testing [12–14]. As a highly accurate non-destructive characterisation technique, it is unsurprising there is already a well-established body of literature utilising *in situ* XRD to characterise crystallographic and thermomechanical properties of varied alloys. *In situ* XRD analysis at varying temperature has been used to establish evolving crystal phase and lattice parameters [15,16], lattice strain (and hence the distribution of stress about crystal systems) [17–20], single crystal elastic constants (SCECs) [21–23], and the nature and density of dislocations generated during deformation [15,24–26]. To the best of our knowledge, high energy *in situ* XRD tensile testing has not been used to characterise the mechanical response of V-based alloys.

Mechanical properties can be concisely evaluated in the form of SCECs, the unique components of the material's elastic tensor from which the whole of a material's elastic response may be evaluated [27]. The single crystal elastic constants of pure vanadium at room temperatures have been experimentally studied using ultra-sonic pulse echoing on specially grown large single crystal samples [28–30]. More common is the theoretical investigation of SCECs using density functional theory (DFT) approaches, which has previously been applied to V-(0-50)Cr-(0-47)Ti alloys [31,32]. It is well known that DFT calculations allow material properties to be determined from the fundamental electronic structure and energy of an atomic structure, giving unique insight into atomic interaction and chemically driven elemental segregation[33–35]. Such results have long been used to supplement experimental data in materials discovery [36,37]. However, DFT results have been found to be substantially improved when used in concert with experimental results [32]. To develop robust systems which are able to accurately calculate material properties, it is necessary to first ensure an experimental basis of results which may be used to augment modelled results exists. Despite the fact DFT based analysis of the elastic properties of V-Cr-Ti alloys already exists, to the best of our knowledge, experimentally determined values for the single crystal elastic constants of the V44 alloy at room and high temperatures have yet to be reported.

In this work, *in situ* real-time XRD characterisation is performed during tensile testing of a V44 alloy at room and elevated temperature (550°C and 700°C), with results being analysed to determine thermomechanical properties, lattice strain evolution and single crystal elastic constants. The results presented in this work serve as a confirmation for the favourable thermomechanical properties of the V44 alloy. Furthermore, these results may be used as a basis from which more complete characterisation of the thermomechanical properties of V-based alloys. The single crystal elastic constants produced can be used to inform future theoretical modelling. DFT results produced using the Vienna Ab initio Simulation (VASP) package are then presented as a point of comparison for experimentally derived SCECs, and as a means of demonstrating the enhancement of DFT results through experimental correction.

2. Materials and Methods

2.1. Materials

The V44 SWIP-30 alloy analysed in this work was supplied by the Southwestern Institute of Physics (SWIP) [8]. A brief summary of the fabrication process first detailed in Fu et al.'s paper [8] is presented here. Over the course of fabrication, a 30kg ingot of SWIP-30 was prepared from >99.95% pure V/Cr/Ti powders, through a process of repeated re-melting, canning, and forming at high vacuum. This process resulted in plates of ~6 mm thickness, which were finally annealed at 1273-1293 K, producing homogeneous plates of high purity. The elemental composition of the alloys ultimately produced are collected in Table 1.

Table 1
Chemical composition of the SWIP-30 V44 plates [8].

Microalloying Element	Composition by wt%
Cr	3.81
Ti	3.92
C	0.013
N	0.002
O	0.027
S	0.002
Al	0.01
Si	0.059
K	<0.005
Fe	0.0053
Mg	0.0022
Ca	0.0067
Ge	<0.001
Mo	0.0035
Na	<0.005
Ta	<0.001
Zr	<0.001
Ni	0.0082

2.2. Experiments

Synchrotron two-dimensional X-ray diffraction of the V44 SWIP-30 alloy was performed *in situ* during tensile testing at room temperature (RT), 550°C, and 700°C at the Joint Engineering, Environmental and Processing (I12-JEEP) beamline, Diamond Light Source Ltd (UK) [38]. A schematic example of the experimental set-up can be seen in Fig. 1a). Flat dog-bone samples for tensile testing (Fig. 1b) were machined from the as-received V44 alloy using electrical discharge machining, and then ground with 1200 grit SiC paper. Tensile tests were conducted in an Instron electrothermal mechanical testing (ETMT) rig, with an applied displacement rate of 0.0003 mm s^{-1} prior to yielding, and 0.0013 mm s^{-1} after yield, measured by a linear variable differential transformer (LVDT). It should be noted that no strain gauge was attached to the sample, and so the strain shown was determined from the displacement measured by the LVDT. This means the strain recorded may be subject to inaccuracy due to displacement caused by extension in the loading array, unrelated to strain in the dogbone gauge length, particularly during initial loading. Temperature was applied through direct resistance heating across the samples. Tensile testing at 700°C failed during plastic deformation, and so analysis of this test is limited to elastic deformation and only the initial onset of plastic deformation. Test temperature was monitored through a type R thermocouple, spot welded to the edge of the dogbone samples at the middle of the gauge length. Diffraction patterns were collected using a large-area (42 × 42 cm) 2D Thales Pixium RF4343 detector with 2880 × 2881 pixel (each pixel 148 × 148 μm), each scan requiring a capture time of 1 s. The size of the monochromatic beam was 0.5 × 0.5 mm^2, with a beam of energy 80.03 keV (wavelength 0.015 nm). A CeO_2 reference sample (NIST Standard Reference Material 674b) was measured for calibration. Data collected from these experiments was analysed using the DAWN Science visualisation and processing software [39] in conjunction with the MATLAB data analysis software for peak fitting. Following tensile testing, fractographs of the tensile sample surfaces were collected using a JEOL JSM-6060 LV Scanning Electron Microscope, operated at 20 keV.

2.3. X-ray data analysis

Appropriate analysis of the XRD data collected during synchrotron experimentation can yield important baseline information as to the crystallographic structure of V44. The DAWN software allowed the intensity of the diffracted pattern to be integrated over two perpendicular 30° increments, producing diffractograms cor-

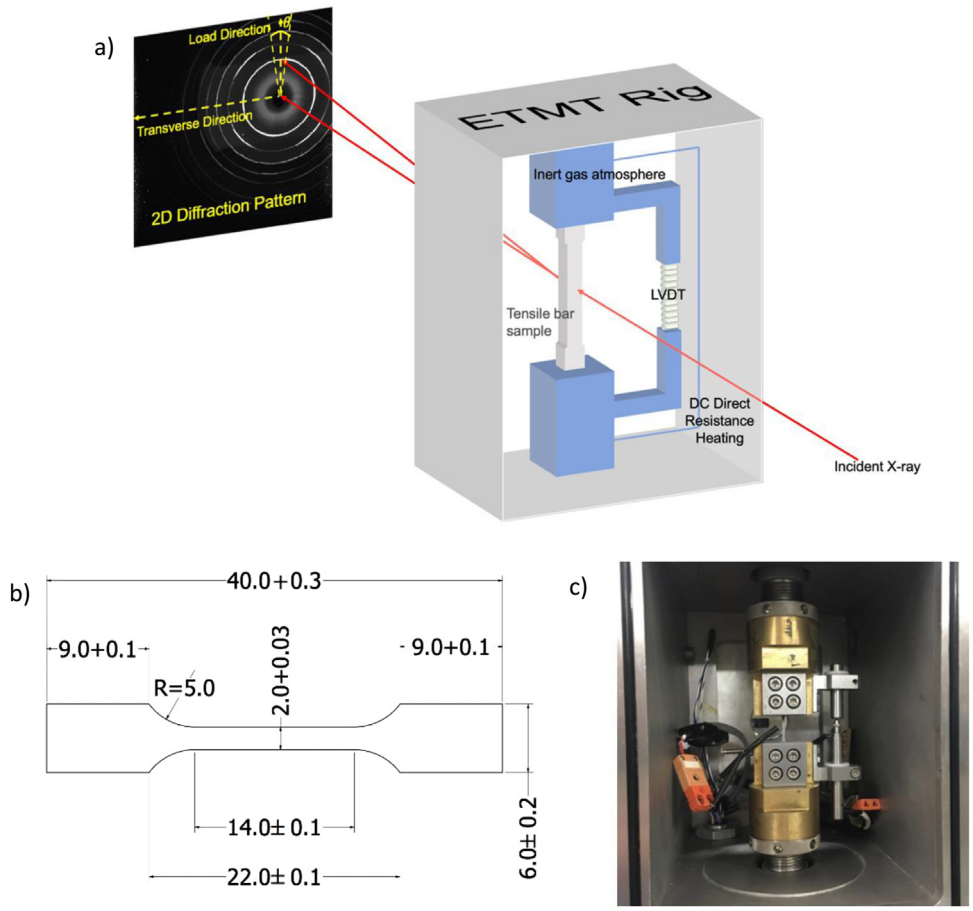

Fig. 1. a) Schematic illustrating the experimental set-up of the in-situ ETMT tensile rig, photographed in c) (labelled angle $\theta = 30^{\circ}$). SubFig. (b) provides dimensions in mm for the dogbone tensile (sample thickness 1.0±0.05 mm) samples machined from V44 for in-situ tensile XRD characterisation

relating to the diffracted beam parallel and perpendicular to the direction of load.

The diffraction peaks were fitted in MATLAB using a Pseudo-Voigt function to accurately record the centroid position, and full width half maxima (FWHM). The Pseudo-Voigt function is a convolution of a Gaussian and Lorentzian function, and is of the form Eq. (1):

$$I(x) = I(0) \cdot \left[\mu \cdot e^{-\pi \frac{(x-x_0)^2}{\beta_G^2}} + (1-\mu) \cdot \frac{1}{\frac{\beta_C^2}{\pi^2} + (x-x_0)^2} \right] + h \quad (1)$$

Where $I(x)$ is the intensity, μ is the fraction of the convolution accounted for by the Gaussian model, x_0 is the peak centre, β_G and β_C are constants associated with the Gaussian and Lorentzian fits respectively, and h is the background intensity.

Further mechanical properties can also be determined from the response of the diffractogram peak positioning to stress. The lattice strain associated with each plane can be determined from Eq. (2),

$$\varepsilon_{hkl} = \frac{d_{hkl} - d_0}{d_o} = \frac{q_0}{q_{hkl}} - 1 \quad (2)$$

where d_0 and q_0 are the initial d spacing of the plane and q-value of the peak centre prior to stress being applied respectively, and d_{hkl} and q_{hkl} are the d spacing and peak centre q-value for a given stress. The diffractograms collected parallel to load exhibit the axial tension experienced by the sample, whilst the diffractograms collected perpendicular to load exhibit the radial compression.

2.4. Elastic constant calculation using density functional theory

The density functional theory (DFT) calculations were conducted using the VASP package [40,41], with the projector augmented wave (PAW) method and the Perdew-Burke-Enzerhof (PBE) generalized gradient functional [42]. The PAW pseudoptentials were used with semi-core electron contribution with 10, 11 and 12 electrons treated as valence for Ti, V and Cr, respectively. The plane wave cut-off energy applied in the calculations was 500 eV. Total energies were computed using a Γ-centered Monkhorst-Pack mesh [43] of k-points in the Brillouin zone, with k-mesh spacing of 0.15 $Å^{-1}$, which corresponds to 4×4×4 Gamma-centred k-point meshes for a 4×4×4 supercell of BCC conventional unit cell containing 128 atoms. The representative structures of V-4Cr-4Ti alloy were obtained using Monte Carlo simulations using the cluster expansion model developed for the Cr-Ta-Ti-V-W system [33]. The disordered and short-range ordered structures were generated at 2000 K and 300 K, respectively. Both structures were optimized allowing the full relaxation of volume, ionic positions and cell shape with forces converged to 0.01 eV/Å. The convergence criterion for total energy was set to 10^{-5} eV/cell. To investigate the effect of the value of lattice parameter on the elastic properties of V-4Cr-4Ti alloy, the disordered structure was additionally optimized with a fixed volume corresponding to the experimentally determined lattice parameter at the room temperature. The elastic constants were calculated by deforming the optimized structure and analysing the corresponding variation of total energy as a function of components of strain [44,45].

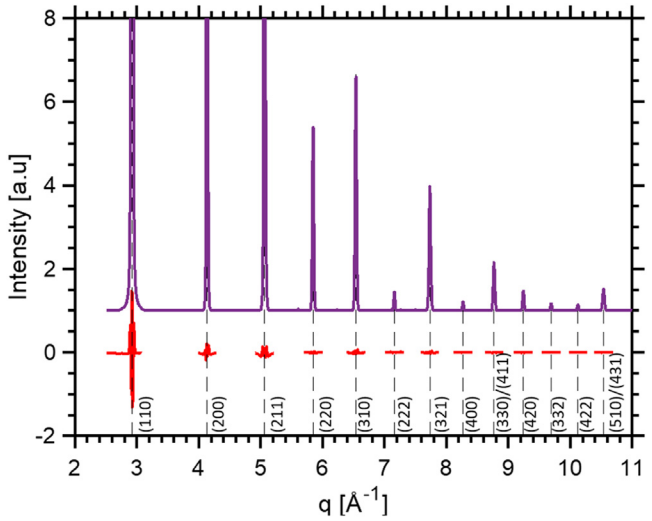

Fig. 2. Example figure showing single diffractogram with the residual after pseudo-voigt fitting plotted below each peak. Diffraction pattern of the sample tested at room temperature analysed over a 30 degree increment centred on the direction of load.

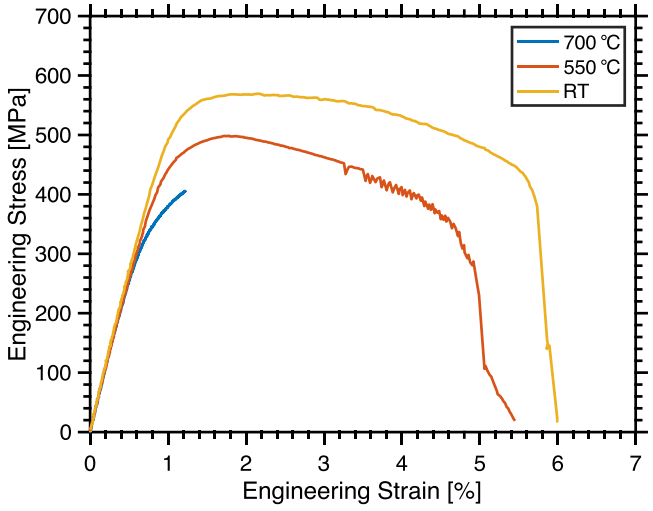

Fig. 3. Engineering stress-strain curve produced during the tensile testing of electron beam melted V44 at varying test temperatures

3. Results and discussion

The results produced in this paper are collected below; with results gathered from crystallographic interrogation prior to load presented first. Lattice strain evolution as a function of stress is presented afterwards and used to calculate single crystal elastic constants (SCECs). These results, in conjunction with SCECs determined through DFT calculations, were used to evaluate the effect of short-range ordering in the alloy and the value of lattice parameter on the elastic properties of the alloy.

3.1. Synchrotron testing

Fig. 2 is an example diffractogram of the kind collected with evolving strain. The matrix phase was confirmed to be body-centred cubic, and this did not transform during heating up to 700°C, or during deformation. The lattice parameter of the room temperature V44 sample was found to be 3.0396 ± 0.0006 Å prior to load, and this result agrees well with previously recorded experimental and theoretical values for this alloy ($\sim 2.994 - 3.03$ Å [46] and 3.000 Å [31]). Error in the peak centre recorded was assessed by considering the effect of pixel size on fit results. Pixel binning limits imposed an error of ± 0.002 Å^{-1} on the x-values recorded, and in order to evaluate the influence of this error on the peak position recorded, peak fitting was performed over one thousand iterations with each x-value randomised within its error bounds. The standard deviation of the histogram yielded from this iterative fitting was used as the error in peak position – this producing a result of approximately ± 0.0006 Å^{-1}, consistent for all peaks.

3.1.1. Thermal expansion

Diffraction data was also recorded during the ramp up from room temperature to test temperature (700°C), during which time no load was applied. Thus, it has been possible to record the lattice parameter-temperature relationship exhibited by the V44 alloy, and in so doing evaluate its thermal expansion coefficient. The thermal expansion coefficient of the alloy was calculated as $10.26 \times 10^{-6} \pm 0.08 \times 10^{-6}$ K^{-1} at 500°C. This compares well to the literature value 10.3×10^{-6} K^{-1} [1], and confirms the favourably low thermal expansion of vanadium alloys when compared to other structural materials under consideration: 18×10^{-6} K^{-1} for 316 stainless steel [1] and 11.9×10^{-6} K^{-1} for oxide dispersion strengthened Eurofer 97 [47].

3.1.2. Tensile testing

The engineering stress-strain relations observed during tensile testing are illustrated in Fig. 3. Using the 0.2% offset method, yield strength was calculated as 525 ± 4 MPa, 450 ± 4 MPa and 359 ± 1 MPa for measurements at room temperature, 550°C, and 700°C respectively whilst the engineering stress corresponding to ultimate tensile strength was found to be 570 MPa at room temperature, and 500 MPa at 550°C. When tested at 550°C, serrations are observed during plastic deformation beyond the ultimate tensile strength; this is likely the result of strain-ageing, by which dislocations move in 'jerky flow' governed by their capture and release by mobile impurities. The presence of this behaviour at elevated temperature may indicate increased dissolution of impurity from precipitates and increased solute impurity mobility. Serrated flow has previously been observed at intermediate temperatures (300-600°C [6,48–52]), and is considered an undesirable effect due to the associated reduction in ductility – upheld here.

Fractographs of the tensile sample surface after fracture at both temperatures are shown in Fig. 4. These figures further demonstrate the character of sample fracture: when tested both at room temperature and 550°C the fracture surfaces exhibited ductile dimples to a degree, indicating semi-ductile fracture. However, the smooth shelf observed in Fig. 4a) indicate a cleavage element to the fracture at room temperature. Similarly, Fig. 4b) exhibits some deviation away from a purely ductile system in the sample tested at 550°C, with the presence of some striations across the sample surface. These striations may be taken as evidence of load cycling, further supporting the presence of strain ageing.

3.1.3. Lattice strain evolution during load-up

The lattice strain-stress relations for each indexed peak are shown graphically in Fig. 5, from which the effect of grain orientation can be interpretated. Prior to yielding, up to stresses approaching 450 MPa in Fig. 5a) 400 MPa in Fig. 5b), and 200 MPa in Fig. 5c), all grain families exhibit a linear response to applied stress corresponding to elastic deformation. From the gradients of this elastic response, the diffraction elastic constant of each sample can be determined. Further, by comparing the positive tensile gradient and negative compressive gradient of the regions of linear extension in these plots, the diffraction elastic ratio can be calcu-

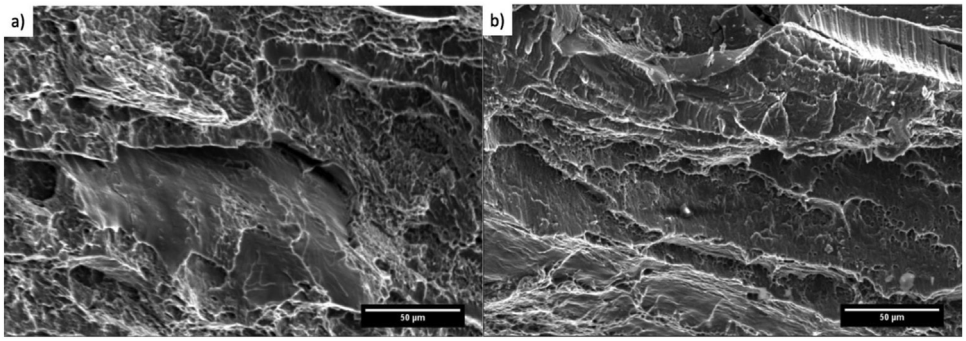

Fig. 4. Fractographs collected from V44 tensile samples tested at a) room temperature and b) 550°C. Both samples demonstrate semi-ductile fracture given the presence, in addition to ductile dimples, of in a) cleavage and in b) striations.

Table 2
Crystal plane specific tensile Diffraction Elastic Constant and Diffraction Elastic Ratio at each test temperature, error included calculated from the error in gradient provided by MATLAB. Blank entries correspond to cases where the diffraction peaks produced were too weak to be accurately recorded.

Lattice Plane	Diffraction Elastic Constant (RT) / GPa	Diffraction Elastic Constant (550°C) / GPa	Diffraction Elastic Constant (700°C) / GPa	Diffraction Elastic Ratio (RT)	Diffraction Elastic Ratio (550°C)	Diffraction Elastic Ratio (700°C)
{110}	125±2	121±2	114±1	0.37±0.03	0.33±0.03	0.35±0.03
{200}	130±1	121±1	125±1	0.38±0.02	0.40±0.01	0.37±0.02
{211}	123.2±0.8	119.3±0.8	114.4±0.6	0.35±0.01	0.37±0.01	0.35±0.01
{220}	130.4±0.8	122.6±0.7	117.1±0.6	0.391±0.009	0.349±0.008	0.377±0.008
{310}	131.1±0.7	120.1±0.6	120.5±0.5	0.378±0.008	0.357±0.007	0.345±0.007
{222}	129.1±0.6		107.7±0.4	0.373±0.007		0.354±0.005
{321}	128.3±0.5	118.6±0.5	113.7±0.4	0.383±0.006	0.372±0.005	0.355±0.005
{420}	131.4±0.5	125.8±0.5		0.387±0.005	0.407±0.004	

lated using Eq. (3), below:

$$\upsilon = {}^{E_{\parallel}}/_{E_{\perp}} \tag{3}$$

where υ is the diffraction elastic ratio, $E_{\parallel}$ and $E_{\perp}$ are the elastic moduli of the lattice plane parallel and perpendicular to the direction of load respectively. The results of this analysis, including diffraction elastic constants and diffraction elastic ratio, are collected in Table 2. Observing both the change in grain family stiffness (measured through diffraction elastic constant), and the onset and degree of non-linearity exhibited by each grain family at elevated temperature, the directional dependency of elastic response can be commented upon.

At room temperature the {222}, {110}, and {211} grain families appeared most elastically compliant, whilst the {200} grain family was elastically stiffest. Approaching bulk yield, it can be seen the planes begin to diverge from linearity; the stiff {200}, {310}, and {330/411} grain families move into plastic deformation at 400 MPa. This yielding causes a redistribution of accumulated stress among the grains, the pre-yield grains experiencing increased stress, and hence increased elastic strain – producing an accompanying non-linear response in the more compliant grain families. There is some variation in lattice plane dependent elastic response with test temperature. At 550°C, all grain families maintain a strongly linear response almost to the point of yield, and even during plastic deformation the deviation in grain family response is only slight. Indeed the diffraction elastic constants produced by the stiffest and most compliant grains only differ by ~6.5 GPa at this temperature. However, at 700°C the relative stiffness of each grain family is more distinct, and the linear response of each grain family breaks down at noticeably different stresses, suggesting a more directionally dependent elastic response at this temperature.

It is important to note there is some notable disagreement between the {110} and {220} curves recorded at room temperature: the diffraction elastic constants recorded being 125 ± 2 GPa and 130.4 ± 0.8 GPa respectively. This disagreement is unphysical as the diffracting planes contributing to both curves are the same, and so the diffraction elastic constants recorded are expected to agree with each other. Whilst the two values only differ by ~5.4 GPa, and so are still in reasonably good objective agreement, they fall significantly outside three standard deviations of one another. This points to an incomplete consideration of error sources within this analysis; the cumulative effects of detector sensitivity, software processing, and material inhomogeneity [53,54] not exhaustively considered, though it must be noted these subtle sources of error are difficult to account for.

3.1.4. Single crystal elastic constants

The polycrystalline elastic diffraction constants associated with each crystallographic plane can be used to evaluate the elastic modulus and single crystal elastic constants (SCECs) of the V44 alloy, using the Kroner model [55]. In this model Eqs. (4)–(7), the diffraction shear modulus, G_{hkl}, follows the relation:

$$G_{hkl}^3 - \alpha G_{hkl}^2 - \beta G_{hkl} - \gamma = 0 \tag{4}$$

Where α, β, and γ are constants ultimately derived from the single crystal elastic constants such that

$$\alpha = \frac{1}{5}(2\eta + 3\mu) - \frac{3}{8}(3K_M + 4(\mu + 3(\eta - \mu)A_{hkl}) \tag{5}$$

$$\beta = \frac{3}{40}(6K_M\eta + 9K_M\mu + 20\eta\mu) - \frac{3K_M}{4}(\mu + 3(\eta - \mu)A_{hkl}) \tag{6}$$

$$\gamma = \frac{3K_M\eta\mu}{4} \tag{7}$$

These equations being expressed in terms of the cubic shear moduli (μ *and* η - Eqs. (9) and (10)), the bulk modulus (K_M - Eq. (8)), and the elastic anisotropy factor (A_{hkl} - Eq. (13)) defined below:

$$K_M = \frac{1}{3}(c_{11} + 2c_{12}) \tag{8}$$

$$\mu = \frac{1}{2}(c_{11} - c_{12}) \tag{9}$$

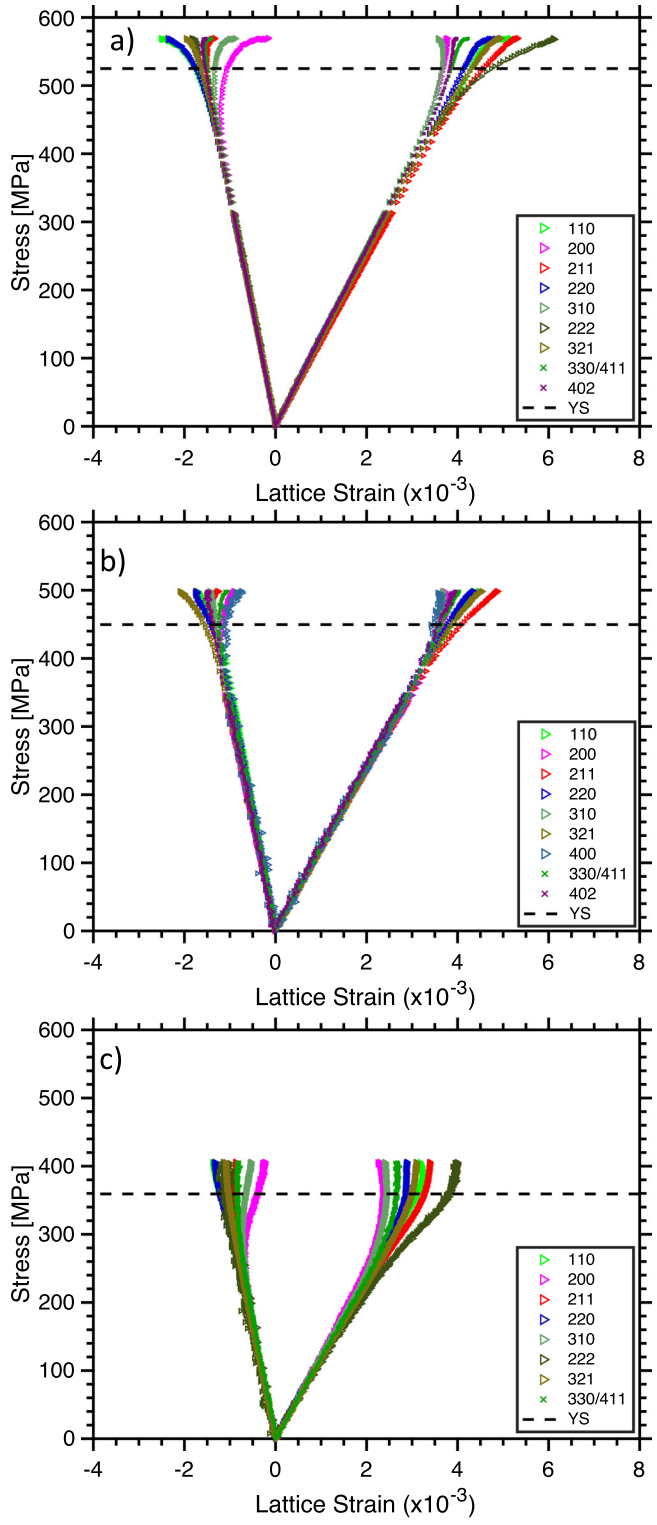

Fig. 5. Figures illustrating the compressive and tensile lattice strain experienced by the sample under stress when tested at a) room temperature, b) 550°C, and c) 700°C, with bulk yield stress (calculated from Fig. 4 by the 0.2% offset method) overlaid.

$$\eta = c_{44} \tag{10}$$

In conjunction with the relation in Eq. (4), the following Kroner model equations Eq. (11) and (12) relating diffraction shear modulus to the experimentally determined diffraction elastic constants, E_{hkl}, and diffraction elastic ratios, ν_{hkl}, were used as a basis for data fitting.

$$\frac{1}{9K_M} - \frac{1}{6G_{hkl}} = -\frac{\nu_{hkl}}{E_{hkl}} \tag{11}$$

$$\frac{1}{G_{hkl}} = 2\left(\frac{1}{E_{hkl}} + \frac{\nu_{hkl}}{E_{hkl}}\right) \tag{12}$$

MATLAB was then used to identify appropriate values for the single crystal elastic constants (and hence α, β, and γ) so as to provide an optimised fit of the experimental data provided, whilst also satisfying the relations given in Eqs. (4), (11), and (12). The fit generated at the three temperatures by the Kroner model is demonstrated graphically in Fig. 6a), Fig. 6d), and Fig. 6g). The single crystal elastic constants corresponding to this fit were then used in the Reuss and Voigt models [55], and the fit produced from these models is overlaid so as to compare the suitability of these models in describing the elastic anisotropy of the sample. It can be observed the Kroner model provides a better fit than the Reuss or Voigt plots, but the variation in the diffraction elastic properties is only slight at room temperature and 550°C– the elastic diffraction constant remains approximately constant over all lattice plane orientations, indicating largely isotropic elasticity, represented graphically in Fig. 6b), c), e), and f).

The single crystal elastic constants produced from this fitting are recorded in Table 3. The error associated with these values was calculated by observing the deviation of each value when the fitting was performed over ten thousand arrays, for which the diffraction elastic constant and diffraction elastic ratio were randomised within their respective error bars. The result at room temperature agrees well with theoretical values previously calculated for V-Cr-Ti alloys (and corrected from existing experimental data); C_{11} previously having been reported on the order $\sim 240-280$ GPa, $C_{12} \sim 110-130$GPa, $C_{44} \sim 36.2-60$ GPa [31,32].

Moreover, the difference in elastic diffraction coefficient between grain orientations provides some indication of Zener anisotropy ratio, when one considers the effect of elastic anisotropy, A_{hkl} – an indexing parameter reliant upon the plane orientations such that:

$$A_{hkl} = \frac{h^2k^2 + k^2l^2 + h^2l^2}{\left(h^2 + k^2 + l^2\right)^2} \tag{13}$$

Whereas the cubic Zener anisotropy ratio, Z, is dependent upon the single crystal elastic constants (C_{11}, C_{12}, C_{44}), defined by the relation shown in Eq. (14):

$$Z = \frac{2c_{44}}{c_{11} - c_{12}} \tag{14}$$

In the case where Z>1 the diffraction elastic coefficient increases as A_{hkl} decreases, whereas when Z<1 the diffraction elastic coefficient increases with A_{hkl}, whilst Z=1 indicates a purely isotropic structure. As can be seen in Table 3 the Z value is 1.0 at both room temperature and 550°C, indicating a very isotropic structure.

The elastic modulus recorded at room temperature is determined as 129.5 ± 0.4 GPa, consistent with the literature values of 121-140 GPa produced from previous analysis of variously fabricated V44 samples [1,56–58]. The change in elastic modulus with increased temperature, is in fairly good agreement with the values suggested by the Young's modulus-temperature dependency previously observed [56,57,59]. In addition to this, whilst the temperature dependency of the Poisson's ratio of V44 has not been investigated, the value produced for Poisson's ratio at room temperature, 0.379 ± 0.008, agrees fairly well with the literature value of 0.36 [1]. The good agreement between these results and previously recorded physical properties provides a source of validation for the data fitting performed on the diffraction data.

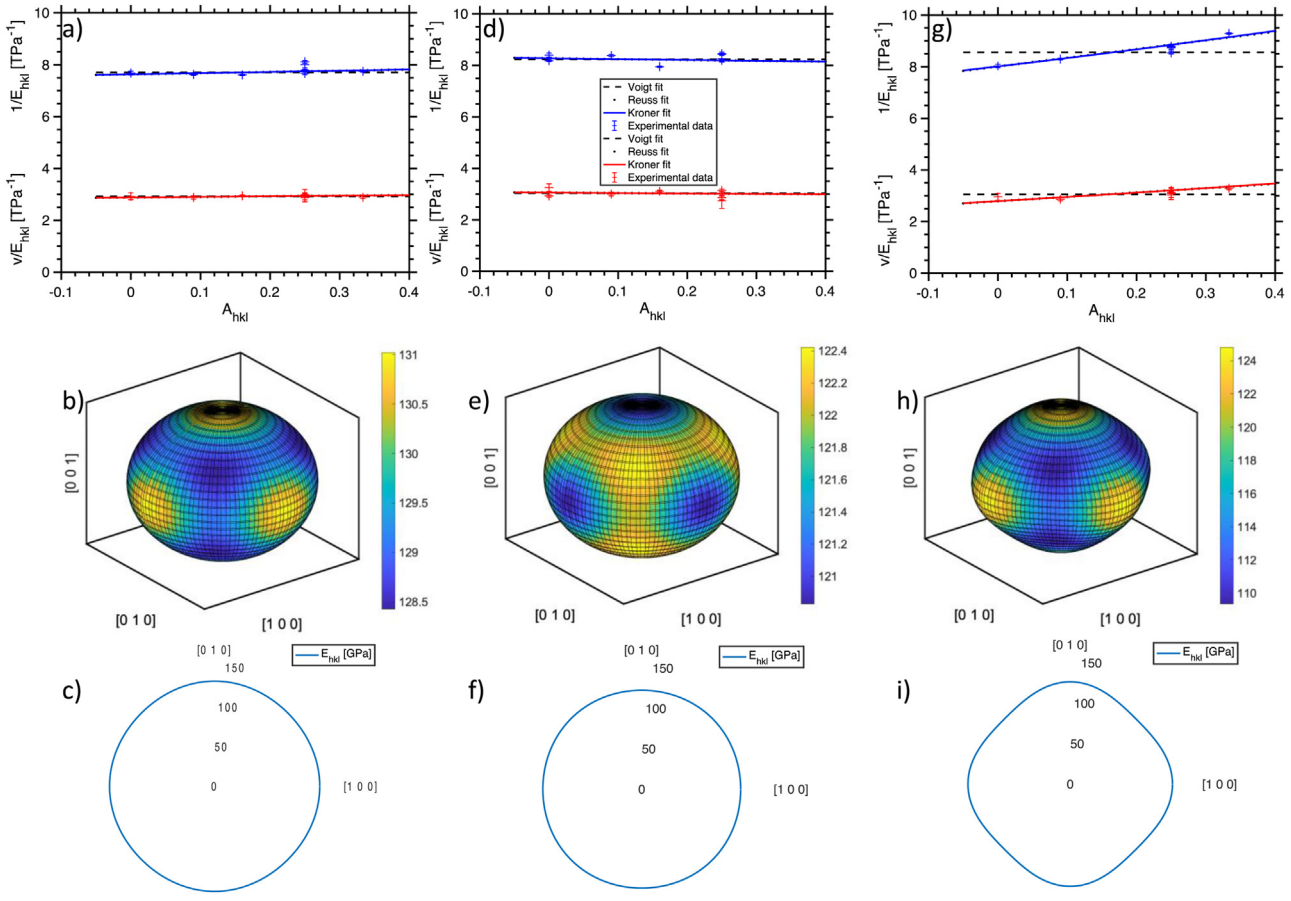

Fig. 6. Figures demonstrating the directional variation of V44's elastic properties: a), b), and c) at room temperature, d), e), and f) at 550°C, g), h), and i) at 700°C. Fig.s a), d), and g) demonstrate the dependency of the plane specific elastic constants on elastic anisotropy including the fit provided by the Voigt, Reuss, and Kroner models used to determine the single crystal elastic constants. The legend provided in Fig. 6d) applies to a), d), and g). Fig.s b), e) and h) show the three dimensional variation of elastic modulus with direction, and Fig.s c), f) and i) are a projection of this modulus-direction dependency onto the XY plane.

Table 3
Comparison of non-zero elastic tensor components and related elastic properties of the V44 alloy determined through experimentation and calculation. All elastic properties and tensor components given in GPa

		C_{11} [GPa]	C_{12} [GPa]	C_{44} [GPa]	Z	υ	Polycrystalline Moduli		
							B [GPa]	G [GPa]	E [GPa]
Calculation	Short-range ordered 300K (a=2.9825 Å)	276.5±0.2	139.4 ±0.1	10.4 ±0.2	0.152	0.45 ±0.03	185.0	24.6	70.3
	Disordered 2000K (a=2.9825 Å)	285.1 ±0.8	136.2 ±0.9	16.5 ±0.3	0.222	0.43 ±0.03	185.9	31.9	90.1
	Disordered 2000K (a=3.0396 Å)	259 ±2	136 ±3	15 ±2	0.24	0.44 ±0.03	177.0	27.5	78.3
Experimental	In situ XRD at 298K	240 ±10	150 ±10	46.0 ±0.2	1.0 ±0.2	0.379 ±0.008	181 ±7	46.9 ±0.2	129.5±0.4
	In situ XRD at 823K	212 ±8	125 ±9	45.1 ±0.2	1.0 ±0.1	0.368 ±0.007	154 ±6	44.5 ±0.2	121.8±0.3
	In situ XRD at 973K	205 ±8	103 ±8	37.3 ±0.2	0.73 ±0.08	0.360 ±0.008	137 ±6	42.4 ±0.2	115.3±0.3

3.2. Density functional theory calculations

The full components of the elastic tensor, calculated in Monte Carlo simulations detailed above, are collected in the Supplementary Material. As expected, the C_{ij} components calculated at room temperature for $i = 1-6$, $j = 4-6$, $i \neq j$ were very close to zero, and the variation between the sets of components C_{11}, C_{22}, and C_{33}, and C_{44}, C_{55}, and C_{66} was very slight – these being features common to cubic symmetry systems. As a result of this, the full tensor components have been condensed to C_{11}, C_{12}, and C_{44}. The single crystal elastic constants and associated elastic properties generated in this way are collected in Table 3. The values for C_{11}, C_{12}, and C_{44} presented in Table 3 are averaged from calculated values of equivalent components: C_{11} from C_{11}, C_{22}, and C_{33}, C_{12} from C_{12}, C_{13}, and C_{23}, and C_{44} from C_{44}, C_{55}, and C_{66}. The polycrystalline shear moduli presented are calculated via the Voigt-Reuss-Hill method Eqs. (15)–(17) such that:

$$G_{VRH} = 0.5 \times \left(G_{Voigt} + G_{Reuss}\right) \tag{15}$$

where

$$G_{Voigt} = \left(1/5\right) \times (C_{11} - C_{12} + 3C_{44}) \quad (16)$$

$$G_{Reuss} = \frac{5}{4(S_{11} - S_{12}) + 3S_{44}} \quad (17)$$

Sij being components of the compliance tensor, defined by [S]=[C]$^{-1}$. The polycrystalline bulk moduli and elastic moduli are then calculated in the same way as reported in Tang et al.'s recent work [60].

3.2.1. Atomic short range ordering

DFT modelling over a range of states, from ordered to disordered, allows the chemical affinity of alloy elements for one another to be evaluated. The configuration of the modelled supercell is recorded through the short-range order (SRO) parameter – this parameter describes the probability of finding pairs of elements within proximity of each other, ie the probability of finding a particular element, *a*, within a set volume around another element, *b*. The SRO parameter is therefore important in determining how the presence of alloying elements influences the lattice structure of the parent element, and predicting elemental segregation within the alloy. This in turn allows a fuller understanding of factors informing alloy mechanical properties to be developed relating underlying atomic structure to changing mechanical response.

SRO parameters were evaluated between pairs of atoms in V-4Cr-4Ti using the combination of Monte Carlo simulations with DFT-based energy model as a function of temperature. This evaluation was performed over the first shell (Fig. 7a), the second shell (Fig. 7b), and the average of both shells (Fig. 7c). The dependency of these parameters on temperature demonstrated that Cr and Ti have a different behaviour within the V host at the low temperature region (Fig. 7). While the SRO parameter behaviour between Cr and Ti is strongly positive, the SRO between V and Cr, and V and Ti become negative. This demonstrates that both Ti and Cr atoms exhibit strong chemical bonding with V, but tend to segregate away from one another. The atomistic structure of V-4Cr-4Ti alloys simulated at 300K by our Monte Carlo simulation is also shown in Fig. 7d. It can be clearly seen in this figure that Ti atoms (in green) and Cr atoms (in blue) are present in segregated clusters throughout the V atoms (in red), with little contact between these clusters.

3.2.2. DFT calculation of elastic constants

Our detailed elastic constant calculations (Table 3) showed only a slight increase of C_{11} and C_{44} for the configuration generated at 300K in a comparison with those at 2000K. This indicates that atomic ordering in the V-4Cr-4Ti alloy does not have a significant influence on its elastic properties and the investigated alloy should maintain similar elastic properties even after long annealing/aging times. As has been previously reported for DFT assessed V and V-rich alloys [27,31], the average elastic constants computed for the fully relaxed structure are quite far from the values measured experimentally. Most notably, the average C_{11} value is strongly overestimated and the average C_{44} value is noticeably underestimated in comparison with the experimental results measured at RT, and this discrepancy can be explained in several ways. Firstly, one important consideration is the impact of distortive sample working experienced by tensile samples, which can be expected to increase disagreement between experimental and DFT predicted microstructure. Whilst a short ranged ordered structure is utilised in DFT modelling at RT, residual mechanical stresses may mean the structure of the non-ideal test sample may be more disordered. Discrepancy between experimental and modelled results therefore comes about simply because the model and experimental sample are not consistent.

Another explanation of such a disagreement is the underestimation of the lattice parameter, which is equal to 2.98 Å for the disordered structure optimized using PBE functional and is almost 0.06 Å smaller than the experimental value at RT. As given in Table 3, the elastic constants computed for the structure with the experimental lattice parameter are noticeably closer to the experimental values. In particular, the C_{11} value is almost 25 GPa less overestimated when the DFT calculations are performed for the experimental lattice parameter instead of the fully relaxed structure. These results show that the elastic constants are strongly related with the value of lattice parameter.

In fact, a significant decrease of C_{11}, and a decrease of C_{12} with increasing lattice parameter is in qualitative agreement with the experimental observations showing the same trends for the sample with increased volume measured at 550°C. The unfortunately high uncertainty in the C_{44} value produced using the experimental lattice parameter makes comparison between these two conditions less clearly defined, but the apparently slight variation in C_{44} produced by the increased lattice parameter is as expected.

In addition to the effect of lattice constant, it should be noted an important feature of the V44 alloy is the presence of Ti(C,O,N) precipitates, which increase the strength of this alloy. The model presented does not include the presence of impurities, and so does not consider the formation or dispersity of such precipitates, leading to an atomic structure which is not an accurate representation of the alloy as tested. When considering the model relative to the experimental data, the titanium content is augmented, and the impurity content is reduced. The lack of significant change in calculated elastic properties over such a large temperature may be related to this lack of precipitation. At 2000K all Ti-precipitates present at 300K would be expected to have long since dissolved, inducing a significant change in elastic properties, not seen in these results. Furthermore, the ductility predicted by the calculated data (read through the Poisson's ratio such that a high Poisson's ratio correlates to high ductility [61]) is significantly enhanced relative to that measured through in-situ tensile testing. It must also be considered that the addition of even small concentrations of oxygen to pure vanadium has been shown to marginally increase measured single crystal elastic constants, elastic modulus, and Poisson's ratio [30]. Previous DFT calculation of the elastic properties of V/Ti(C,O,N) heterostructures has indicated the introduction of small volumetric percentages of TiC only weakly increases the elastic modulus, whereas the introduction of many V-TiC interfaces markedly increases the elastic modulus [62]. Whilst the significant difference in atomic structures considered between the current results and the referenced work limits the extent to which quantitative comparisons can be applied, qualitatively both results point to the importance of Ti(C,O,N) type precipitates when considering elastic properties. The presence of oxygen in the vanadium alloy, then, has significant effects on the elastic properties, and some disparity between experimental results and any model which cannot account for this is to be expected.

Previous work has also reported a discrepancy between experimental and theoretically determined elastic properties of vanadium [63–66] – specifically underestimation of vanadium's trigonal shear elastic constant (C_{44}) and hence misestimation of its polycrystalline elastic properties. This underestimation has been linked to the complex electronic structure of vanadium, including an electronic topological transition in the metal's Fermi surface with a significantly weakening effect on shear elastic properties under ambient pressure [67,68], and thermally induced broadening of the Fermi surface which produces anomalous shear behaviour [69,70]. Whilst the underestimation of C_{44} reported here is more severe than in other DFT calculation works concerning vanadium [31,66], the methodology applied in this work (higher cut-off wave energy and more accurate exchange-correlation functional) should return

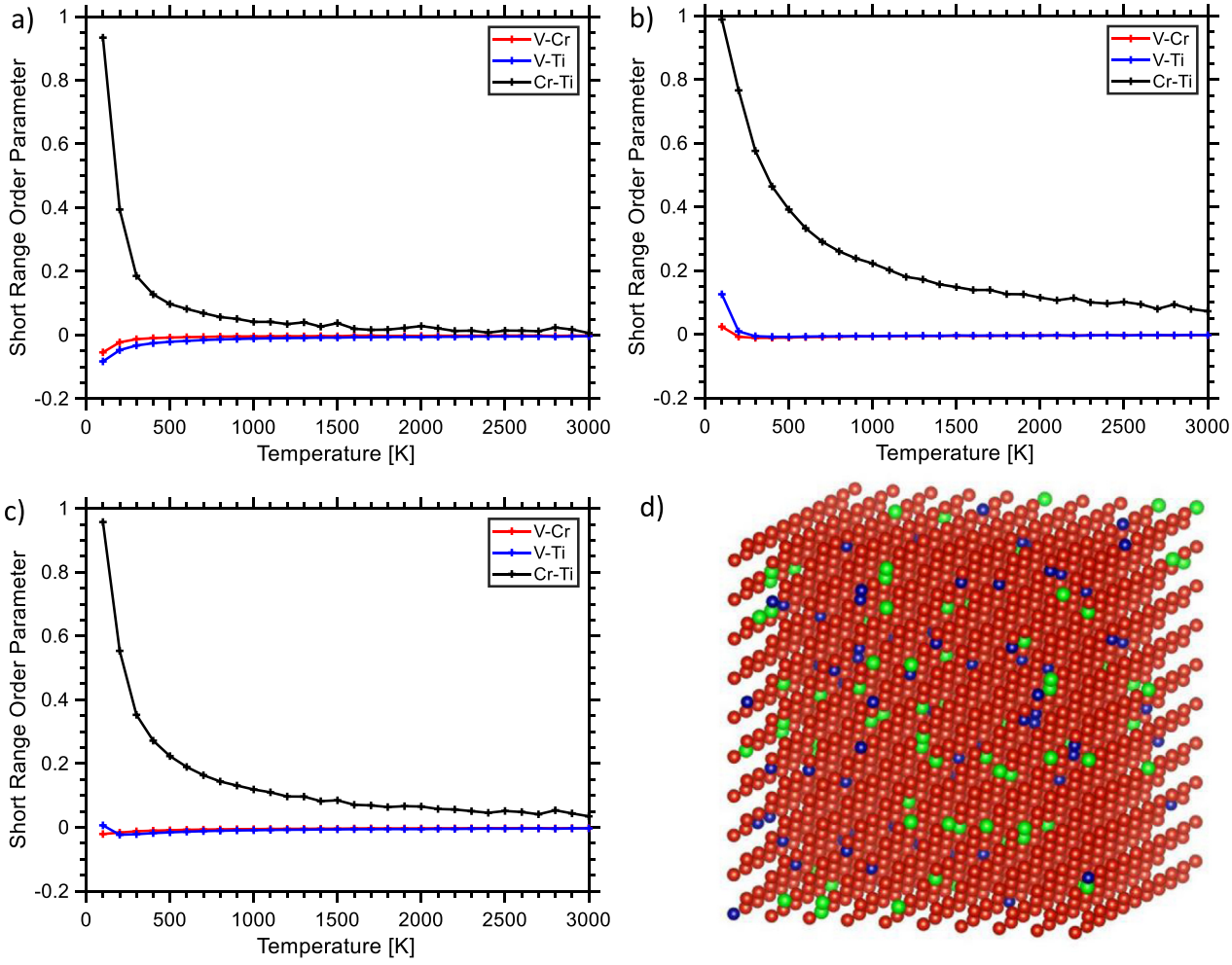

Fig. 7. Fig.s depicting the influence of temperature on the short range order parameter corresponding to a) the first shell, b) the second shell, and c) the average of the two shells, and d) the atomic cell structure generated from Monte Carlo simulation using the DFT energy model (red – V, blue – Cr, green – Ti)

a more accurate model. Indeed, a similarly severe C_{44} underestimation was seen in other work using high cut-off wave energies for a variety of functionals [63,64], and in the Materials Project [27,71]. This suggests the poor agreement between the theoretical and experimental results presented here is attributable, not to inaccuracy in the model applied, but rather to the challenging structure of vanadium.

Such considerations emphasize the importance of experimental characterisation of such values – both as a means to circumvent complex modelling issues, and to inform and assess future models. Whilst current DFT results have allowed for the fundamental effects of solute addition to be better understood through the SRO effects, the inclusion of impurities and the use of experimentally determined parameters to fine tune modelling must be explored to produce more accurate DFT modelled results. Future work therefore requires further experimental determination of material properties, and the construction of more comprehensive theoretical models.

4. Conclusions

The mechanical properties of electron beam melted V44 were investigated using synchrotron XRD analysis of *in situ* tensile testing, at room and high temperature. These test temperatures allowed the confirmation of V44's suitable thermomechanical properties, including a measured linear thermal expansion coefficient of 10.3×10^{-6} K^{-1}. The effective elastic properties of V44 determined from experiment at room temperature were consistent with existing literature, including a Poisson's ratio value of 0.378, and an elastic modulus of 127.8 GPa. The key point of interest can be said to be the determination of the single crystal elastic constants, C_{11}, C_{12}, and C_{44}, which are commonly used in the mechanical modelling of materials. At room temperature these were found to be 240 GPa, 150 GPa, and 46.0 GPa respectively, whilst at 550°C these were determined as 212 GPa, 125 GPa, and 45.0 GPa, and at 700°C, 205 GPa, 103 GPa, and 37.3 GPa. The decrease in single crystal elastic constants with increasing temperature produced a fall in bulk moduli properties that was consistent with existing literature concerning the V44 alloy. The elastic properties calculated through DFT-Monte Carlo simulation were found to be in poor agreement with the experimental results presented: the calculated polycrystalline elastic modulus at room temperature, 70.3 GPa, differing significantly from the experimentally determined value of 129.5 GPa. This disagreement was proposed as the result of the base element's complex electronic structure, paired with lattice parameter mis-estimation, and precipitation behaviour currently unaccounted for. Results produced demonstrated the effectiveness of DFT modelling in elucidating fundamental atomic interactions, and the need for experimental qualification when applying these principles to macroscopic properties.

Declaration of Competing Interest

The authors declare that they have no known competing financial interests or personal relationships that could have appeared to influence the work reported in this paper.

CRediT authorship contribution statement

Tay Sparks: Data curation, Formal analysis, Investigation, Software, Visualization, Writing – original draft, Writing – review & editing. **Duc Nguyen-Manh:** Data curation, Formal analysis, Investigation, Methodology, Project administration, Resources, Software, Writing – original draft, Writing – review & editing, Visualization. **Pengfei Zheng:** Resources, Writing – review & editing. **Jan S. Wróbel:** Formal analysis, Investigation, Writing – review & editing. **Damian Sobieraj:** Formal analysis, Investigation, Writing – review & editing. **Michael Gorley:** Conceptualization, Resources, Supervision, Writing – review & editing. **Thomas Connolley:** Data curation, Investigation, Resources, Writing – review & editing. **Christina Reinhard:** Data curation, Investigation, Resources, Writing – review & editing. **Yiqiang Wang:** Conceptualization, Data curation, Funding acquisition, Investigation, Methodology, Project administration, Supervision, Writing – review & editing, Resources. **Biao Cai:** Conceptualization, Data curation, Funding acquisition, Investigation, Methodology, Project administration, Supervision, Writing – review & editing, Resources.

Data Availability

Data will be made available on request.

Acknowledgements

Funding for this work was provided by the United Kingdom Atomic Energy Authority (UKAEA) and the University of Birmingham, School of Metallurgy & Materials. We acknowledge the Diamond Light Source for time on the I12 beamline under proposal [EE19251]. The authors thank the University of Manchester for access to the ETMT rig. Dr Wang, Dr Gorley and Dr. Nguyen-Manh (DNM) would also like to acknowledge the EPSRC grants EP/T012250/1 and EP/W006839/1, and the UK Government Department for Business, Energy & Industrial Strategy. Work of DNM, Jan S. Wróbel (JSW) and Damian Sobieraj (DS) has been carried out within the framework of the EUROfusion Consortium, funded by the European Union via the Euratom Research and Training Programme (Grant Agreement No 101052200 — EUROfusion). Views and opinions expressed are however those of the author(s) only and do not necessarily reflect those of the European Union or the European Commission. Neither the European Union nor the European Commission can be held responsible for them. DNM and JSW also acknowledges the support from high-performing computing facility MARCONI (Bologna, Italy) provided by EUROfusion. The work at Warsaw University of Technology has been carried out as a part of an international project co-financed from the funds of the program of the Polish Minister of Science and Higher Education entitled "PMW" in 2019, Agreement No. 5018 / H2020-Euratom / 2020/2. The simulations were also carried out with the support of the Interdisciplinary Centre for Mathematical and Computational Modelling (ICM), University of Warsaw, under grant No. GB79-6.

Supplementary materials

Supplementary material associated with this article can be found, in the online version, at doi:10.1016/j.jnucmat.2022.153911.

References

[1] D.L. Smith, H.M. Chung, B.A. Loomis, H. Matsui, S. Votinov, W. Van Witzenburg, Development of vanadium-base alloys for fusion first-wall-blanket applications, Fusion Eng. Des. 29 (C) (1995) 399–410.
[2] D.L. Smith, M.C. Billone, S. Majumdar, R.F. Mattas, D.K. Sze, Materials integration issues for high performance fusion power systems, J. Nucl. Mater. 258–263 (1998) 65–73 PART 1 A.
[3] T. Muroga, J.M. Chen, V.M. Chernov, R.J. Kurtz, M.Le Flem, Present status of vanadium alloys for fusion applications, J. Nucl. Mater. 455 (1–3) (2014) 263–268.
[4] T. Muroga, Vanadium alloys for fusion blanket applications, Mater. Trans. 46 (3) (2005) 405–411.
[5] D.. Diercks, B.A. Loomis, 1. Introduction, J. Nucl. Mater. 143 (1986) 1117–1124.
[6] B.A. Loomis, R.H. Lee, D.L. Smith, J.R. Peterson, Strength, ductility, and ductile-brittle transition temperature for MFR candidate vanadium alloys, J. Nucl. Mater. 155–157 (2) (1988) 631–638 PART.
[7] H.M. Chung, B.A. Loomis, D.L. Smith, Properties of V4Cr4Ti for application as fusion reactor structural components, Fusion Eng. Des. 29 (C) (1995) 455–464.
[8] H.Y. Fu, et al., Fabrication using electron beam melting of a V-4Cr-4Ti alloy and its thermo-mechanical strengthening study, J. Nucl. Mater. 442 (1-3) (2013) S336 SUPPL.1.
[9] J.M. Chen, V.M. Chernov, R.J. Kurtz, T. Muroga, Overview of the vanadium alloy researches for fusion reactors, J. Nucl. Mater. 417 (1–3) (2011) 289–294.
[10] K. Sakai, M. Satou, M. Fujiwara, K. Takanashi, A. Hasegawa, K. Abe, Mechanical properties and microstructures of high-chromium V-Cr-Ti type alloys, J. Nucl. Mater. 329–333 (2004) 457–461 no. 1-3 PART A.
[11] F. Laliberte, M. Li, J. Almer, L. Liu, In-situ synchrotron X-ray study of microstructural evolution during creep deformation in Grade 91 steel, Mater. Sci. Eng. A 737 (2018) 115–123 September.
[12] B. Sun, T. Shen, Probing the deformation mechanisms of nanocrystalline silver by in-situ tension and synchrotron x-ray diffraction, Metals (Basel) 10 (12) (2020) 1–14.
[13] G. Zhang, et al., The evolution of internal stress and dislocation during tensile deformation in a 9Cr ferritic/martensitic (F/M) ODS steel investigated by high-energy X-rays, J. Nucl. Mater. 467 (2015) 50–57.
[14] A. Bénéteau, P. Weisbecker, G. Geandier, E. Aeby-Gautier, B. Appolaire, Austenitization and precipitate dissolution in high nitrogen steels: An in situ high temperature X-ray synchrotron diffraction analysis using the Rietveld method, Mater. Sci. Eng. A 393 (1–2) (2005) 63–70.
[15] X. Zhang, et al., In situ high-energy X-ray diffraction study of tensile deformation of neutron-irradiated polycrystalline Fe-9%Cr alloy, Acta Mater 126 (2017) 67–76.
[16] R. Blondé, et al., High-energy X-ray diffraction study on the temperature-dependent mechanical stability of retained austenite in low-alloyed TRIP steels, Acta Mater 60 (2) (2012) 565–577.
[17] Y. Miao, et al., Load-partitioning in an oxide dispersion-strengthened 310 steel at elevated temperatures, Mater. Des. 111 (2016) 622–630.
[18] B. Clausen, T. Lorentzen, M.A.M. Bourke, M.R. Daymond, Lattice strain evolution during uniaxial tensile loading of stainless steel, Mater. Sci. Eng. A 259 (1) (1999) 17–24.
[19] B. Clausen, Characterisation of Polycrystal Deformation, Riso Natl. Lab. Roskilde ISBN 985 (1997) 1 September.
[20] D. Kiefer, J. Gibmeier, A. Stark, Determination of temperature-dependent elastic constants of steel AISI 4140 by use of in situ x-ray dilatometry experiments, Materials (Basel) 13 (10) (2020).
[21] C. Lee, et al., Lattice distortion in a strong and ductile refractory high-entropy alloy, Acta Mater 160 (2018) 158–172.
[22] Z. Wang, A.D. Stoica, D. Ma, A.M. Beese, Diffraction and single-crystal elastic constants of Inconel 625 at room and elevated temperatures determined by neutron diffraction, Mater. Sci. Eng. A 674 (2016) 406–412.
[23] Y. Wu, et al., Phase Stability and Deformation Behavior of TiZrHfNbO High-Entropy Alloys, Front. Mater. 7 (2020) 1–7 November.
[24] Z. Fan, B. Jóni, G. Ribárik, É. Ódor, Z. Fogarassy, T. Ungár, The Microstructure and strength of a V–5Cr–5Ti alloy processed by high pressure torsion, Mater. Sci. Eng. A 758 (2019) 139–146 March.
[25] X. Zhang, et al., High-energy synchrotron x-ray study of deformation-induced martensitic transformation in a neutron-irradiated Type 316 stainless steel, Acta Mater 200 (2020) 315–327.
[26] C. Xu, et al., In-situ high-energy X-ray characterization of neutron irradiated HT-UPS stainless steel under tensile deformation, Acta Mater 156 (2018) 330–341.
[27] M. De Jong, et al., Charting the complete elastic properties of inorganic crystalline compounds, Sci. Data 2 (2015) 1–13.
[28] G.A. Alers, Elastic Moduli of Vanadium, Network 119 (5) (1960) 1532–1535.
[29] D.I. Bolef, R.E. Smith, J.G. Miller, Elastic properties of vanadium. I. Temperature dependence of the elastic constants and the thermal expansion, Phys. Rev. B 3 (12) (1971) 4100–4108.
[30] J.D. Greiner, O.N. Carlson, J.F. Smith, Single-crystal elastic constants of vanadium and vanadium with oxygen additions, J. Appl. Phys. 50 (6) (1979) 4394–4398.
[31] X. Li, et al., Elastic properties of vanadium-based alloys from first-principles theory, Phys. Rev. B - Condens. Matter Mater. Phys. 86 (1) (2012).
[32] J. Fu, X. Li, B. Johansson, J. Zhao, Improved Finnis-Sinclair potential for vanadium-rich V–Ti–Cr ternary alloys, J. Alloys Compd. 705 (2017) 369–375.

[33] D. Sobieraj, et al., Chemical short-range order in derivative Cr-Ta-Ti-V-W high entropy alloys from the first-principles thermodynamic study, Phys. Chem. Chem. Phys. 22 (41) (2020) 23929–23951.
[34] Y. Ikeda, B. Grabowski, F. Körmann, Ab initio phase stabilities and mechanical properties of multicomponent alloys: A comprehensive review for high entropy alloys and compositionally complex alloys, Mater. Charact. 147 (2018) 464–511 June2019.
[35] E. Kiely, R. Zwane, R. Fox, A.M. Reilly, S. Guerin, Density functional theory predictions of the mechanical properties of crystalline materials, CrystEngComm 23 (34) (2021) 5697–5710.
[36] K. Alberi, et al., The 2019 materials by design roadmap, J. Phys. D. Appl. Phys. 52 (2019).
[37] Y. Liu, T. Zhao, W. Ju, S. Shi, S. Shi, S. Shi, Materials discovery and design using machine learning, J. Mater. 3 (3) (2017) 159–177.
[38] T. Connolley, C.M. Beavers, P. Chater, High-Energy Adventures at Diamond Light Source, Synchrotron Radiat. News 33 (6) (2020) 31–36.
[39] J. Filik, et al., Processing two-dimensional X-ray diffraction and small-angle scattering data in DAWN 2, J. Appl. Crystallogr. 50 (3) (2017) 959–966.
[40] G. Kresse, J. Furthmuller, Effecient iterative schemes for ab initio total energy calculations using a plane-wave basis set, Phys. Rev. B 54 (16) (1996) 11169–11183.
[41] G. Kresse, J. Furthmüller, Efficiency of ab-initio total energy calculations for metals and semiconductors using a plane-wave basis set, Comput. Mater. Sci. 6 (1) (1996) 15–50.
[42] J.P. Perdew, K. Burke, M. Ernzerhof, Generalized gradient approximation made simple, Phys. Rev. Lett. 77 (18) (1996) 3865–3868.
[43] H. Monkhorst, J. Pack, Special points for Brillouin-zone integrations, Phys. Rev. B 13 (12) (1976) 5188–5192.
[44] J.S. Wróbel, et al., Elastic dipole tensors and relaxation volumes of point defects in concentrated random magnetic Fe-Cr alloys, Comput. Mater. Sci. 194 (2021).
[45] J. F. Nye, *Physical Properties of Crystals - Their Representation Tensors and Matrices*. 1986.
[46] Z.D. Li, Q. Li, Y. Li, T.D. Ma, Microstructure and properties of V–5Cr–5Ti alloy after hot forging, Fusion Eng. Des. 127 (2) (2018) 83–90.
[47] P. Norajitra, Divertor Development for a Future Fusion Power Plant 7 (2) (2011).
[48] M. Satou, K. Abe, H. Kayano, High-temperature deformation of modified V-Ti-Cr-Si type alloys, J. Nucl. Mater. 179–181 (1) (1991) 757–761 PART.
[49] T. Miyazawa, et al., Effect of yttrium on dynamic strain aging of vanadium alloys, J. Nucl. Mater. 442 (1-3) (2013) S341–S345 SUPPL.1.
[50] S.J. Zinkle, et al., Research and development on vanadium alloys for fusion applications, J. Nucl. Mater. 258–263 (1998) 205–214 PART 1 A.
[51] D.L. Harrod, R.E. Gold, Mechanical properties of vanadium and vanadium-base alloys, Int. Met. Rev. 25 (1) (1980) 163–211.
[52] L.L. Snead, D.T. Hoelzer, M. Rieth, A.A.N. Nemith, Refractory Alloys: Vanadium, Elsevier Inc., Niobium, Molybdenum, Tungsten, 2019.
[53] E.T.C. Filho, J.T.N. Medeiros, L.G. Martinez, V.C. Pinto, Study of Error Analysis and Sources of Uncertainty in the Measurement of Residual Stresses by the X-Ray Diffraction, Residual Stress. 2018 6 (2018) 75–80.
[54] C. Simpson, D. Knowles, M. Mostafavi, Influence of Microstructure on Synchrotron X-ray Diffraction Lattice Strain Measurement Uncertainty, Metals (Basel) 11 (774) (2021).
[55] R. De Wit, Diffraction elastic constants of a cubic polycrystal, J. Appl. Crystallogr. 30 (4) (1997) 510–511.
[56] B.K. Kardashev, V.M. Chernov, Internal friction, plastic properties, and impact toughness of V-Ti-Cr alloys, Phys. Solid State 50 (5) (2008) 854–859.
[57] B.K. Kardashev, V.M. Chernov, O.A. Plaskin, V.A. Stepanov, L.P. Zavialski, Internal friction and Young's modulus of V-Ti-Cr alloy before, during and after proton irradiation, J. Alloys Compd. 310 (1–2) (2000) 102–106.
[58] H. Luo, et al., The effect of yttrium addition on the microstructure and irradiation hardening in V-4Cr-4Ti alloy under self-ion irradiation, Metals (Basel) 11 (7) (2021).
[59] D. Hancock, D. Homfray, M. Porton, I. Todd, B. Wynne, Refractory metals as structural materials for fusion high heat flux components, J. Nucl. Mater. 512 (2018) 169–183.
[60] L. Tang, et al., Deformation mechanisms of FeCrNi medium entropy alloy at 293 and 15 K, Acta Mater (2022).
[61] G.N. Greaves, A.L. Greer, R.S. Lakes, T. Rouxel, Poisson's ratio and modern materials, Nat. Mater. 10 (11) (2011) 823–837.
[62] X. Zhang, et al., Precipitate/vanadium interface and its strengthening on the vanadium alloys: A first-principles study, J. Nucl. Mater. 527 (2019) 151821.
[63] Y.X. Wang, H.Y. Geng, Q. Wu, X.R. Chen, Orbital localization error of density functional theory in shear properties of vanadium and niobium, J. Chem. Phys. 152 (2) (2020).
[64] N. Nagasako, M. Jahnátek, R. Asahi, J. Hafner, Anomalies in the response of V, Nb, and Ta to tensile and shear loading: Ab initio density functional theory calculations, Phys. Rev. B - Condens. Matter Mater. Phys. 81 (9) (2010) 1–13.
[65] P. Söderlind, O. Eriksson, J.M. Wills, A.M. Boring, Theory of elastic constants of cubic transition metals and alloys, Phys. Rev. B 48 (9) (1993) 5844–5851.
[66] Y.L. Liu, H.B. Zhou, Y. Zhang, Ideal mechanical properties of vanadium by a first-principles computational tensile test, J. Nucl. Mater. 416 (3) (2011) 345–349.
[67] L. Koči, Y. Ma, A.R. Oganov, P. Souvatzis, R. Ahuja, Elasticity of the superconducting metals V, Nb, Ta, Mo, and W at high pressure, Phys. Rev. B - Condens. Matter Mater. Phys. 77 (21) (2008) 1–5.
[68] A. Landa, et al., Fermi surface nesting and pre-martensitic softening in v and Nb at high pressures, J. Phys. Condens. Matter 18 (22) (2006) 5079–5085.
[69] F.C. Yang, O. Hellman, B. Fultz, Temperature dependence of electron-phonon interactions in vanadium, Phys. Rev. B 101 (9) (2020).
[70] E. Walker, Anomalous Temperature Behaviour of the Shear Elastic Constant C44 in Vanadium, Solid State Commun 28 (1978) 587–589.
[71] A. Jain, et al., Commentary: The materials project: A materials genome approach to accelerating materials innovation, APL Mater 1 (1) (2013).